Jpn. J. Appl. Phys. Vol. 40 (2001) pp. 4753–4762
Part 1, No. 7, July 2001

Cross-Sectional Elastic Imaging of Arterial Wall Using Intravascular Ultrasonography

Hitoshi MITA, Hiroshi KANAI, Yoshiro KOIWA[1], Masataka ICHIKI[2] and Fumiaki TEZUKA[3]

Graduate School of Engineering, Tohoku University, Sendai 980-8579, Japan
[1]*Graduate School of Medicine, Tohoku University, Sendai 980-8574, Japan*
[2]*JR Sendai Hospital, Itsutsubashi 1-1-5, Sendai 980-8508, Japan*
[3]*Sendai National Hospital, Miyagino 2-8-8, Sendai 983-8520, Japan*

(Received November 23, 2000; accepted for publication April 16, 2001)

There have been several studies on the imaging of the distribution of the elasticity of the arterial wall using intravascular ultrasonography (IVUS). In those studies, the elasticity is estimated only during ventricular diastole. However, the viscous characteristics of the smooth muscle in the media of the arterial wall are also included in the strain measured during diastole. Alternatively, during systole, the smooth muscle has an almost purely elastic characteristic. However, the IVUS probe moves greatly due to the arrival of the pulsatile wave at the beginning of the ejection period. Therefore, in this paper, we propose a method to compensate for the movement of the IVUS probe in order to precisely measure the regional change in thickness of the arterial wall during one cardiac cycle. Basic experiments using a silicone rubber tube, in which pulsatile flow is generated by an artificial heart, determined the two-dimensional (2-D) distribution of the regional change in thickness and the elasticity. The obtained incremental elastic modulus coincides with that determined by the static pressure-strain test. Furthermore, in an *in vitro* experiment performed on an extracted human iliac artery, the 2-D distribution of elasticity is obtained and compared with pathological results.

KEYWORDS: cross-sectional elastic image, intravascular ultrasonography (IVUS), atherosclerosis

1. Introduction

The number of serious circulatory diseases such as myocardial infarction and cerebral infarction has recently increased. These diseases are mainly caused by the rupture of an unstable atherosclerotic plaque. Since the elasticity of the arterial wall, on which the atherosclerotic plaque is formed, is highly dependent on its tissue properties,[1)] evaluation of the regional elasticity of the arterial wall has the potential for supplying useful information for diagnosis of the vulnerability of atherosclerotic plaque.

In conventional intravascular ultrasonography (IVUS), the cross-sectional B-mode image of the artery is obtained by inserting the IVUS probe into the artery and rotating the probe in order to scan the ultrasonic beam. From the B-mode image, the size and shape of the atherosclerotic plaque on the arterial wall can be observed. For calcified tissue, the intensity of the reflective wave generally increases and is highly apparent on the B-mode image.[2)] For lipid-rich plaque or fibrous plaque, however, it is difficult to discriminate them from normal tissue based on the B-mode image obtained by conventional IVUS.

Several studies have been conducted where cross-sectional images of the elasticity of the arterial wall have been obtained using IVUS.[3–6)] In those studies, elasticity is estimated only during ventricular diastole. However, both elastic and viscous characteristics of the smooth muscle in the media, which is dominant in the arterial wall, are included in the strain measured during ventricular diastole.[7)] Therefore, the strain measurement should be conducted during ventricular systole when the smooth muscle has an almost purely elastic characteristic. However, the IVUS probe moves greatly due to the pulsatile flow during the ejection period. Therefore, each point along the arterial wall should be tracked before measuring the change in thickness or the strain.

In addition, when the IVUS probe is inserted into the artery, the inner pressure around the IVUS probe is reduced due to the occlusion of the arterial lumen caused by blood flow. It is, therefore, necessary to compensate for the inner pressure measured near the IVUS probe.

In this experiment, a new method is proposed for accurately measuring the change in thickness of the arterial wall by tracking the wall position. Moreover, a method for compensating for the inner pressure is proposed. The elasticity of the arterial wall is obtained from the measured change in thickness. The proposed method is validated by basic experiments using a water tank to estimate the change in thickness, and the cross-sectional image of the elasticity is obtained in an *in vitro* experiment performed on an extracted human iliac artery.

2. Principle

2.1 Tracking the instantaneous position of the arterial wall

At the beginning of the ejection period, the IVUS probe moves greatly due to the arrival of the pulsatile wave since the IVUS probe cannot be fixed in place in the artery. The motion of the IVUS probe causes displacement and rotation in the 2-D cross-sectional image of the IVUS.

In the IVUS system employed in this experiment, the period of one rotation of the IVUS probe, ΔT, is 33 ms, which is called the *frame interval*. The maximum displacement of the IVUS probe in the actual artery is about 10 μm during the frame interval ΔT. Thus, we assume that the cross-sectional shape of the artery and its center position $O(t)$ do not change during each short frame interval ΔT.

The initial inner radius $R(t_0; \theta_0)$ and the wall thickness $h(t_0; \theta_0)$ for each angle θ_0 ($0 \leq \theta_0 < 2\pi$) were set at time t_0, as shown in Fig. 1(a). Multiple measurement points $\{P(r_0, \theta_0)\}$ were set with a constant interval Δr from the inner surface of the artery along the ultrasonic beam with an angle θ_0 at time t_0, where r_0 denotes the distance of the point $P(r_0, \theta_0)$ from the center position $O(t_0)$ of the IVUS probe, as shown in Fig. 1(b). Since 360° is divided into 512 angles in the employed IVUS, the resolution $\Delta\theta$ for detecting the

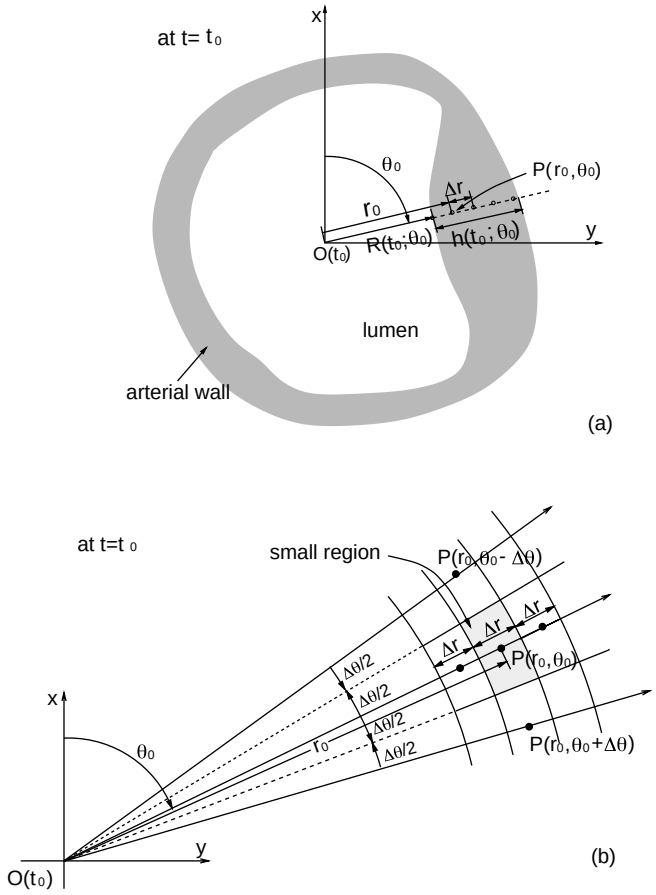

Fig. 1. Multiple measurement points and small regions. (a) The set of multiple measurement points $\{P(r_0, \theta_0)\}$. $P(r_0, \theta_0)$ was set at constant interval Δr at time t_0. (b) The small regions were set for the change in thickness $\Delta h(t; P(r_0, \theta_0))$ around each point $P(r_0, \theta_0)$ with a thickness of $\pm\Delta r/2$ and an angle of $\pm\Delta\theta/2$.

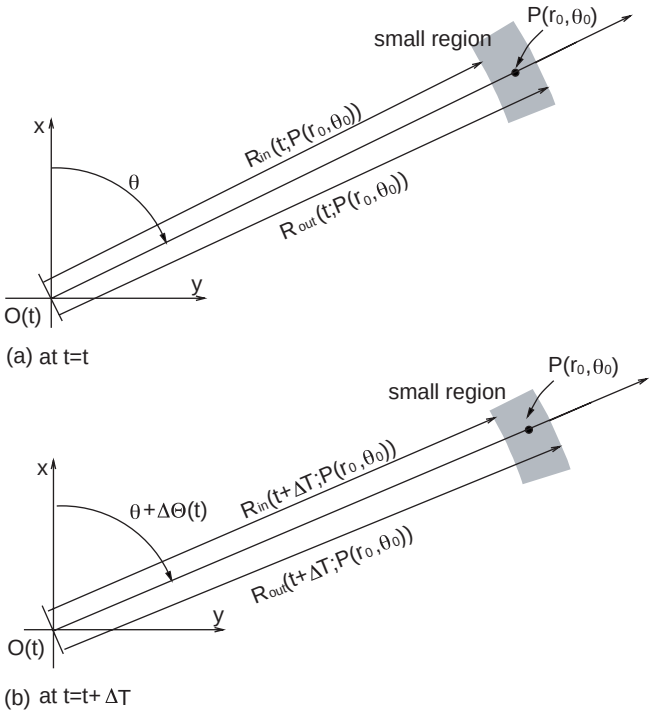

Fig. 2. Change in the distances of the inner and outer surfaces of the small region around point $P(r_0, \theta_0)$ from the center position $O(t)$ of the IVUS probe (a) at $t = t$ and (b) $t = T + \Delta T$.

rotation $\Delta\Phi$ during ΔT is 0.7°. A small region was set with thickness of $\pm\Delta r/2$ and angle of $\pm\Delta\theta/2$ around each point $P(r_0, \theta_0)$, as shown in Fig. 1(b). We tracked the movement of each point $P(r_0, \theta_0)$ during ΔT and obtained the change in thickness of the small region around $P(r_0, \theta_0)$ as follows. We assumed that during the frame interval ΔT from time t, the IVUS probe rotated by $\Delta\Theta(t)$, and that the distances from the center position $O(t)$ of the IVUS probe to the inner and outer surfaces of the small region around point $P(r_0, \theta_0)$ changed from $R_{\text{in}}(t; P(r_0, \theta_0))$ to $R_{\text{in}}(t + \Delta T; P(r_0, \theta_0))$ and from $R_{\text{out}}(t; P(r_0, \theta_0))$ to $R_{\text{out}}(t + \Delta T; P(r_0, \theta_0))$, respectively, as shown in Fig. 2. The changes in $R_{\text{in}}(t; P(r_0, \theta_0))$ and $R_{\text{out}}(t; P(r_0, \theta_0))$ during ΔT are respectively given by

$$\Delta R_{\text{in}}(t; P(r_0, \theta_0)) = R_{\text{in}}(t + \Delta T; P(r_0, \theta_0)) - R_{\text{in}}(t; P(r_0, \theta_0)), \tag{2.1}$$

$$\Delta R_{\text{out}}(t; P(r_0, \theta_0)) = R_{\text{out}}(t + \Delta T; P(r_0, \theta_0)) - R_{\text{out}}(t; P(r_0, \theta_0)). \tag{2.2}$$

Using the complex cross-correlation function, $\alpha(t; \Delta\Phi)$, between the echo signals reflected by the entire arterial wall at time t and those of the succeeding frame at time $t+\Delta T$, rotation $\Delta\Theta(t)$ of the IVUS probe and the displacement, $\Delta R_{\text{in}}(t; P(r_0, \theta_0))$ and $\Delta R_{\text{out}}(t; P(r_0, \theta_0))$, of point $P(r_0, \theta_0)$ during ΔT are determined as follows.

Let us denote the quadrature-demodulated echo signal reflected by the object at a distance r from the center $O(t)$ of the IVUS probe and an angle θ at time t by $y(t; r, \theta)$. Rotation $\Delta\Theta(t)$ of the IVUS probe during the frame interval ΔT from t to $t + \Delta T$ is determined from that which maximizes the following magnitude of the complex cross-correlation function, $\alpha(t; \Delta\Phi)$, between $y(t; r, \theta)$ received at time t and $y(t + \Delta T; r, \theta)$ received at time $t + \Delta T$:

$$\alpha(t; \Delta\Phi) = \frac{\left| \sum_{\substack{R(t;\theta_0)-L \le r \le R(t;\theta_0)+L \\ 0 \le \theta < 2\pi}} y^*(t; r, \theta)\, y(t + \Delta T; r, \theta + \Delta\Phi) \right|}{\sqrt{\sum_{\substack{R(t;\theta_0)-L \le r \le R(t;\theta_0)+L \\ 0 \le \theta < 2\pi}} |y(t; r, \theta)|^2} \sqrt{\sum_{\substack{R(t;\theta_0)-L \le r \le R(t;\theta_0)+L \\ 0 \le \theta < 2\pi}} |y(t + \Delta T; r, \theta + \Delta\Phi)|^2}}, \tag{2.3}$$

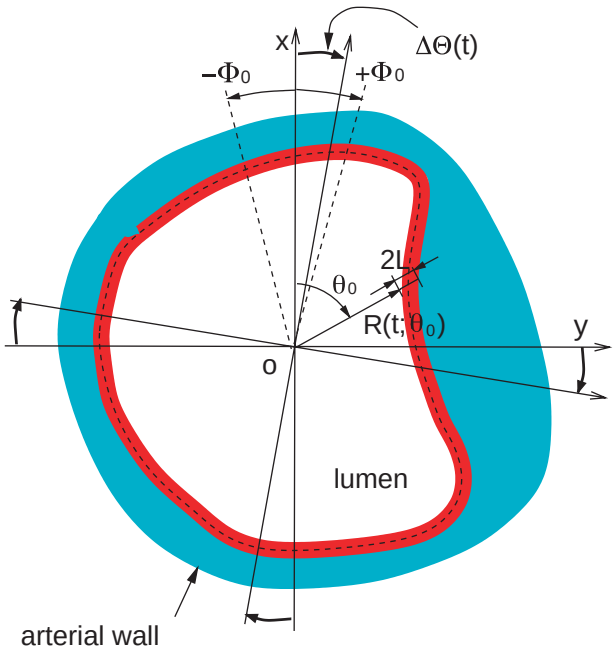

Fig. 3. Estimation of rotation $\Delta\Theta(t)$ of the IVUS probe during frame interval ΔT by maximizing the cross-correlational function, $\alpha(t;\Delta\Phi)$, of the quadrature-demodulated echo signals.

where $\pm L$ is the window length in the radial direction around the initial inner surface $R(t;\theta_0)$, as shown in Fig. 3. For various values $\{\Delta\Phi\}$ of $-\Phi_0 \le \Delta\Phi \le +\Phi_0$, $\{\alpha(t;\Delta\Phi)\}$ are calculated and rotation $\Delta\Theta(t)$ of the IVUS probe during ΔT is estimated from their maximum values as follows.

$$\alpha\left(t;\widehat{\Delta\Theta}(t)\right) = \max_{-\Phi_0\le\Delta\Phi\le+\Phi_0} \alpha(t;\Delta\Phi), \tag{2.4}$$

where Φ_0 is equal to 7° and L is equal to 225 μm in the following experiments.

The change in thickness, $\Delta h(t;P(r_0,\theta_0))$, in the small region around point $P(r_0,\theta_0)$ set at time t_0, is estimated from the difference between the displacement $\Delta R_{\rm in}(t;P(r_0,\theta_0))$ at the inner surface and the displacement $\Delta R_{\rm out}(t;P(r_0,\theta_0))$ at the outer surface of the small region as

$$\widehat{\Delta h}(t;P(r_0,\theta_0)) = \widehat{\Delta R}_{\rm out}(t;P(r_0,\theta_0)) - \widehat{\Delta R}_{\rm in}(t;P(r_0,\theta_0)). \tag{2.5}$$

For this purpose, the instantaneous positions of $R_{\rm in}(t;P(r_0,\theta_0))$ and $R_{\rm out}(t;P(r_0,\theta_0))$ are tracked as follows. From the complex cross-correlation function between the quadrature-demodulated echo signals, $y(t;r,\theta)$ and $y(t+\Delta T;r,\theta)$, the phase shift, $\Delta\varphi_{\rm in}(t;P(r_0,\theta_0))$, at the inner surface $R_{\rm in}(t;P(r_0,\theta_0))$ and the phase shift, $\Delta\varphi_{\rm out}(t;P(r_0,\theta_0))$, at the outer surface $R_{\rm in}(t;P(r_0,\theta_0))$ of the small region around point $P(r_0,\theta_0)$ are estimated by

$$\widehat{\Delta\varphi}_{\rm in}(t;P(r_0,\theta_0)) = \angle C_{\rm in}(t;P(r_0,\theta_0)), \tag{2.6}$$

$$\widehat{\Delta\varphi}_{\rm out}(t;P(r_0,\theta_0)) = \angle C_{\rm out}(t;P(r_0,\theta_0)), \tag{2.7}$$

where $\angle C_{\rm in}(t;P(r_0,\theta_0))$ and $\angle C_{\rm out}(t;P(r_0,\theta_0))$ are the phases of the complex cross-correlation functions, $C_{\rm in}(t;P(r_0,\theta_0))$ and $C_{\rm out}(t;P(r_0,\theta_0))$, respectively, between the signal $y(t;r,\theta)$ reflected at point $P(r_0,\theta_0)$ at time t and the signal $y(t+\Delta T;r,\theta)$ reflected at time $t+\Delta T$, and the rotation angle is corrected by $\widehat{\Delta\Theta}(t)$ estimated in eq. (2.4). The complex cross-correlation functions $C_{\rm in}(t;P(r_0,\theta_0))$ and $C_{\rm out}(t;P(r_0,\theta_0))$ are respectively averaged around the surfaces $R_{\rm in}(t;P(r_0,\theta_0))$ and $R_{\rm out}(t;P(r_0,\theta_0))$ and they are given by

$$\begin{aligned} C_{\rm in}(t;P(r_0,\theta_0)) = {} & \frac{1}{D_{\rm in}(t;P(r_0,\theta_0))} \\ & \times \sum_{\substack{-\frac{\delta}{2}\le\Delta r\le+\frac{\delta}{2}\\ -\frac{\omega}{2}\le\Delta\theta\le+\frac{\omega}{2}}} \left\{ y^*\left(t;\widehat{R}_{\rm in}(t;P(r_0,\theta_0))+\Delta r,\theta_0+\Delta\theta\right)\right. \\ & \left. \times y\left(t+\Delta T;\widehat{R}_{\rm in}(t;P(r_0,\theta_0))+\Delta r,\theta_0+\Delta\theta+\widehat{\Delta\Theta}(t)\right)\right\}, \end{aligned} \tag{2.8}$$

$$\begin{aligned} C_{\rm out}(t;P(r_0,\theta_0)) = {} & \frac{1}{D_{\rm out}(t;P(r_0,\theta_0))} \\ & \times \sum_{\substack{-\frac{\delta}{2}\le\Delta r\le+\frac{\delta}{2}\\ -\frac{\omega}{2}\le\Delta\theta\le+\frac{\omega}{2}}} \left\{ y^*\left(t;\widehat{R}_{\rm out}(t;P(r_0,\theta_0))+\Delta r,\theta_0+\Delta\theta\right)\right. \\ & \left. \times y\left(t+\Delta T;\widehat{R}_{\rm out}(t;P(r_0,\theta_0))+\Delta r,\theta_0+\Delta\theta+\widehat{\Delta\Theta}(t)\right)\right\}, \end{aligned} \tag{2.9}$$

where

$$\begin{aligned} D_{\rm in}(t;P(r_0,\theta_0)) = {} & \sqrt{\sum_{\substack{-\frac{\delta}{2}\le\Delta r\le+\frac{\delta}{2}\\ -\frac{\omega}{2}\le\Delta\theta\le+\frac{\omega}{2}}} \left| y\left(t;\widehat{R}_{\rm in}(t;P(r_0,\theta_0))+\Delta r,\theta_0+\Delta\theta\right)\right|^2} \\ & \times \sqrt{\sum_{\substack{-\frac{\delta}{2}\le\Delta r\le+\frac{\delta}{2}\\ -\frac{\omega}{2}\le\Delta\theta\le+\frac{\omega}{2}}} \left| y\left(t+\Delta T;\widehat{R}_{\rm in}(t;P(r_0,\theta_0))+\Delta r,\theta_0+\Delta\theta+\widehat{\Delta\Theta}(t)\right)\right|^2}, \end{aligned} \tag{2.10}$$

$$D_{\mathrm{out}}(t;\, P(r_0,\theta_0)) = \sqrt{\sum_{\substack{-\frac{\delta}{2}\le\Delta r\le+\frac{\delta}{2}\\ -\frac{\omega}{2}\le\Delta\theta\le+\frac{\omega}{2}}} \left| y\left(t;\, \widehat{R}_{\mathrm{out}}(t;\, P(r_0,\theta_0)) + \Delta r, \theta_0 + \Delta\theta\right)\right|^2} \times \sqrt{\sum_{\substack{-\frac{\delta}{2}\le\Delta r\le+\frac{\delta}{2}\\ -\frac{\omega}{2}\le\Delta\theta\le+\frac{\omega}{2}}} \left| y\left(t+\Delta T;\, \widehat{R}_{\mathrm{out}}(t;\, P(r_0,\theta_0)) + \Delta r, \theta_0 + \Delta\theta + \widehat{\Delta\Theta}(t)\right)\right|^2}, \tag{2.11}$$

and δ and ω respectively denote the window widths for the radial direction and the circumferential direction of the small region around surfaces $R_{\mathrm{in}}(t;\, P(r_0,\theta_0))$ and $R_{\mathrm{out}}(t;\, P(r_0,\theta_0))$, as shown in Fig. 4.

Therefore, the instantaneous displacement $\Delta R_{\mathrm{in}}(t;\, P(r_0,\theta_0))$ at the inner surface and $\Delta R_{\mathrm{out}}(t;\, P(r_0,\theta_0))$ at the outer surface of the small region around $P(r_0,\theta_0)$ during the frame interval ΔT are respectively estimated by

$$\widehat{\Delta R}_{\mathrm{in}}(t;\, P(r_0,\theta_0)) = \frac{c}{4\pi f_0}\widehat{\Delta\varphi}_{\mathrm{in}}(t;\, P(r_0,\theta_0)), \tag{2.12}$$

$$\widehat{\Delta R}_{\mathrm{out}}(t;\, P(r_0,\theta_0)) = \frac{c}{4\pi f_0}\widehat{\Delta\varphi}_{\mathrm{out}}(t;\, P(r_0,\theta_0)), \tag{2.13}$$

where c denotes the sound velocity in tissue and is assumed to be 1,540 m/s and f_0 is the center frequency of the employed ultrasound (10 MHz).

By repeating these operations from eq. (2.3) to eq. (2.13) for each frame and by accumulating the resultant instantaneous displacements $\Delta R_{\mathrm{in}}(t;\, P(r_0,\theta_0))$ and $\Delta R_{\mathrm{out}}(t;\, P(r_0,\theta_0))$, the distance $R_{\mathrm{in}}(t;\, P(r_0,\theta_0))$ of the inner surface and $R_{\mathrm{out}}(t;\, P(r_0,\theta_0))$ of the outer surface of the small region from the center position $O(t)$ of the IVUS probe are respectively tracked as

$$\widehat{R}_{\mathrm{in}}(t;\, P(r_0,\theta_0)) = \left(r_0 - \frac{\Delta r}{2}\right) + \sum_{t=t_0}^{t}\widehat{\Delta R}_{\mathrm{in}}(t;\, P(r_0,\theta_0)), \tag{2.14}$$

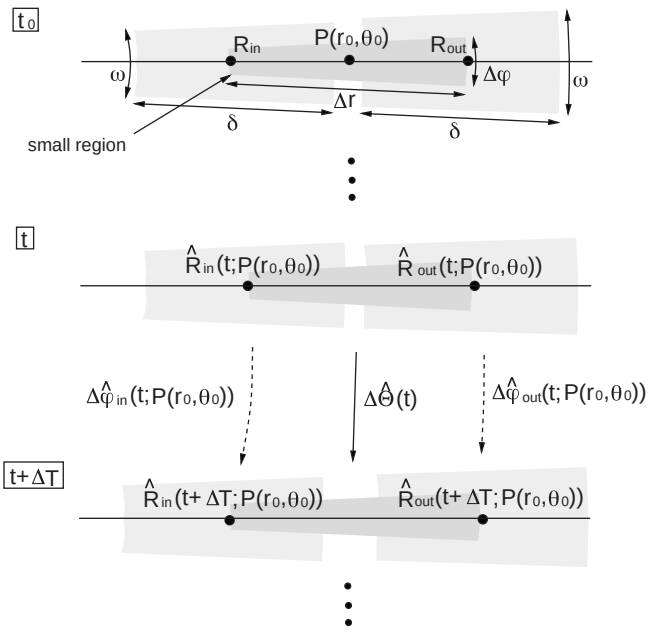

Fig. 4. Estimation of the phase shift, $\Delta\varphi_{\mathrm{in}}(t;\, P(r_0,\theta_0))$, at the inner surface $R_{\mathrm{in}}(t;\, P(r_0,\theta_0))$ and $\Delta\varphi_{\mathrm{out}}(t;\, P(r_0,\theta_0))$ at the outer surface $R_{\mathrm{out}}(t;\, P(r_0,\theta_0))$ of the small region around point $P(r_0,\theta_0)$.

$$\widehat{R}_{\mathrm{out}}(t;\, P(r_0,\theta_0)) = \left(r_0 + \frac{\Delta r}{2}\right) + \sum_{t=t_0}^{t}\widehat{\Delta R}_{\mathrm{out}}(t;\, P(r_0,\theta_0)). \tag{2.15}$$

From the difference between the estimated instantaneous displacements $\widehat{\Delta R}_{\mathrm{in}}(t;\, P(r_0,\theta_0))$ and $\widehat{\Delta R}_{\mathrm{out}}(t;\, P(r_0,\theta_0))$, the change in thickness, $\widehat{\Delta h}(t;\, P(r_0,\theta_0))$, of the small region around point $P(r_0,\theta_0)$ is given by eq. (2.5).

2.2 Calculation of elasticity of the arterial wall

As shown in the hysteresis loop of Fig. 5, during ventricular diastole, the arterial wall has both elastic and viscous properties. During ventricular systole, however, the strain caused by the increase in blood pressure has an almost purely elastic property. In this experiment, therefore, the elastic property of the arterial wall is estimated during ventricular systole as follows.

The instantaneous strain in the radial direction, $\widehat{\varepsilon}_r(t;\, P(r_0,\theta_0))$, in the small region around point $P(r_0,\theta_0)$ set at time t_0 is obtained by

$$\widehat{\varepsilon}_r(t;\, P(r_0,\theta_0)) = \frac{\widehat{\Delta h}(t;\, P(r_0,\theta_0))}{h_d(r_0,\theta_0)}, \tag{2.16}$$

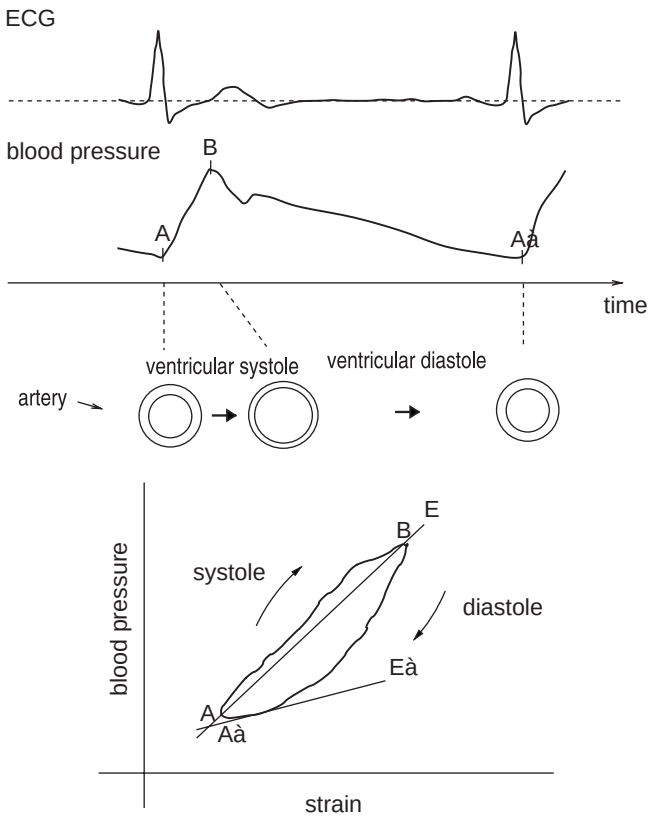

Fig. 5. Smooth muscle during one cardiac cycle.

where $\widehat{\Delta h}(t; P(r_0, \theta_0))$ is estimated using eq. (2.5) and $h_d(r_0, \theta_0)$ is the initial thickness of $R_{\text{out}}(t_0; P(r_0, \theta_0)) - R_{\text{in}}(t_0; P(r_0, \theta_0)) = \Delta r$ in the small region around point $P(r_0, \theta_0)$ at end-diastole, when the blood pressure reaches its minimum. From the ratio of the difference (pulse pressure) Δp in Pa between the maximum blood pressure and the minimum blood pressure during one cardiac cycle to the maximum $\varepsilon_{\text{rm}}(r_0, \theta_0)$ of the resultant strain $\widehat{\varepsilon_r}(t; P(r_0, \theta_0))$ during one cardiac cycle, the elastic modulus $E_\theta(r_0, \theta_0)$ in Pa in the circumferential direction of the small region around point $P(r_0, \theta_0)$ is given by[8)]

$$E_\theta(r_0, \theta_0) = \frac{1}{2}\left(\frac{r}{\Delta r} + 1\right)\frac{\Delta p}{\varepsilon_{\text{rm}}(r_0, \theta_0)}, \tag{2.17}$$

where distribution of the regional stress is not taken in consideration and it is assumed that the stress in the radial direction is homogeneously applied to the arterial wall.

2.3 *Compensating for the measured inner pressure under pulsatile flow*

Due to the insertion of the IVUS probe and/or the atherosclerotic plaque at point B in Fig. 6, the cross-sectional area, S_A, of the lumen at point A is reduced to S_B at point B. Based on the continuity of fluid flow Q along the artery, which is the product of the cross-sectional area S_i and the flow velocity v_i at point i ($i = A, B$), the following equation is given.

$$S_A \cdot v_A = S_B \cdot v_B = Q, \tag{2.18}$$

where the flow velocity is assumed to remain constant for the short duration at the beginning of the ejection period[10)] and $S_A > S_B$. Based on the Bernoulli theorem, on the other hand,

$$\frac{1}{2}\rho v_A^2 + p_A = \frac{1}{2}\rho v_B^2 + p_B, \tag{2.19}$$

where ρ denotes the density of the fluid. From eq. (2.18), $v_A < v_B$. Thus, the pressure p_A at point A is higher than the actual pressure p_B at the IVUS probe.

From eqs. (2.18) and (2.19), the pressure p_B at point B is obtained from the pressure p_A and the flow velocity v_A at point A as follows.

$$p_B = p_A + \frac{1}{2}\rho v_A^2\left\{1 - \left(\frac{S_A}{S_B}\right)^2\right\} \tag{2.20}$$

Thus, the actual pressure p_B at point B is corrected using pressure p_A and velocity v_A, both measured at point A.

Figure 7 shows the actual geometry of the measurement

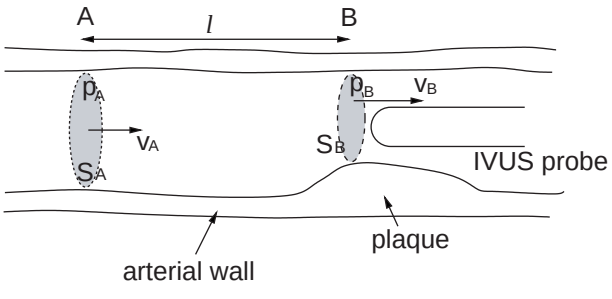

Fig. 6. Decreased cross-sectional area caused by the occlusion resulting from the insertion of the IVUS probe and/or the atherosclerotic plaque.

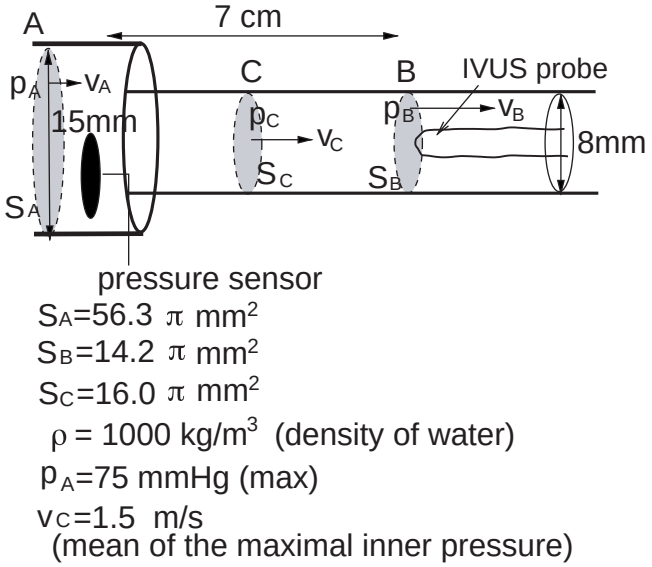

Fig. 7. Geometry of the IVUS probe at point B and the pressure sensor at point A in the silicone rubber tube of Fig. 12.

points in the experimental setup employed in the following experiments using a water tank for estimating the regional change in thickness of a silicone rubber tube. The pressure sensor and the IVUS probe are placed at point A and point B, respectively, as shown in Fig. 7. However, the flow velocity at points A and B cannot be measured in the actual system. Thus, the flow velocity v_C at point C is measured using the conventional ultrasonic FFT-Doppler method. In this experimental setup, the pressure p_B at point B is estimated as follows. From the continuity of fluid flow Q along the artery,

$$S_A \cdot v_A = S_B \cdot v_B = S_C \cdot v_C = Q, \tag{2.21}$$

where S_C is the cross-sectional area at point C. Thus, the flow velocity v_A at point A is given by

$$v_A = \frac{S_C}{S_A}v_C. \tag{2.22}$$

By substituting this equation into eq. (2.20), the pressure p_B at point B is obtained from the pressure p_A measured at point A corrected by the flow velocity v_C measured at point C as follows.

$$p_B = p_A + \frac{\rho}{2}\left\{\left(\frac{S_C}{S_A}\right)^2 - \left(\frac{S_C}{S_B}\right)^2\right\}v_C^2 \tag{2.23}$$

2.4 *Experimental system*

Figure 8 shows the experimental system for measuring the change in thickness of the arterial wall. The detailed specifications of the IVUS probe of the intravascular ultrasonic diagnostic equipment (Aloka, SSD-550) are shown in Table I. In the following experiments, the IVUS probe is rotated with a speed of 30 rotations/s and 2π radian is divided into 512 angles.

2.5 *Pulse width of the employed ultrasonic beam*

The pulse width of the employed ultrasound is measured using a hydrophone. As shown in Fig. 9(a), the hydrophone is set at a distance of 3 mm from the center of the IVUS transducer. The hydrophone moved along the x-axis as shown in

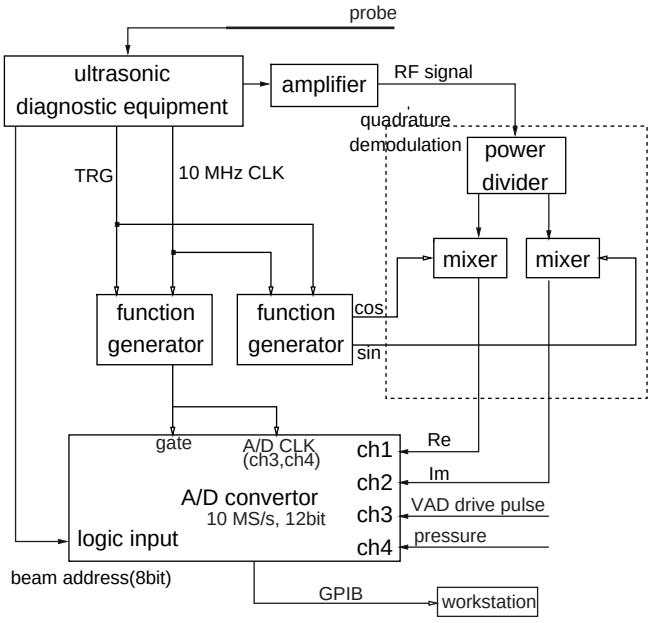

Fig. 8. Block diagram of the employed experimental system.

Table I. Specifications of the square transducer of the employed IVUS probe.

Center frequency f_0	10 MHz
Material	PZT
Size	1.6 mm × 1.6 mm
Thickness	0.22 mm
Diameter of the IVUS probe	8 F (2.7 mm)

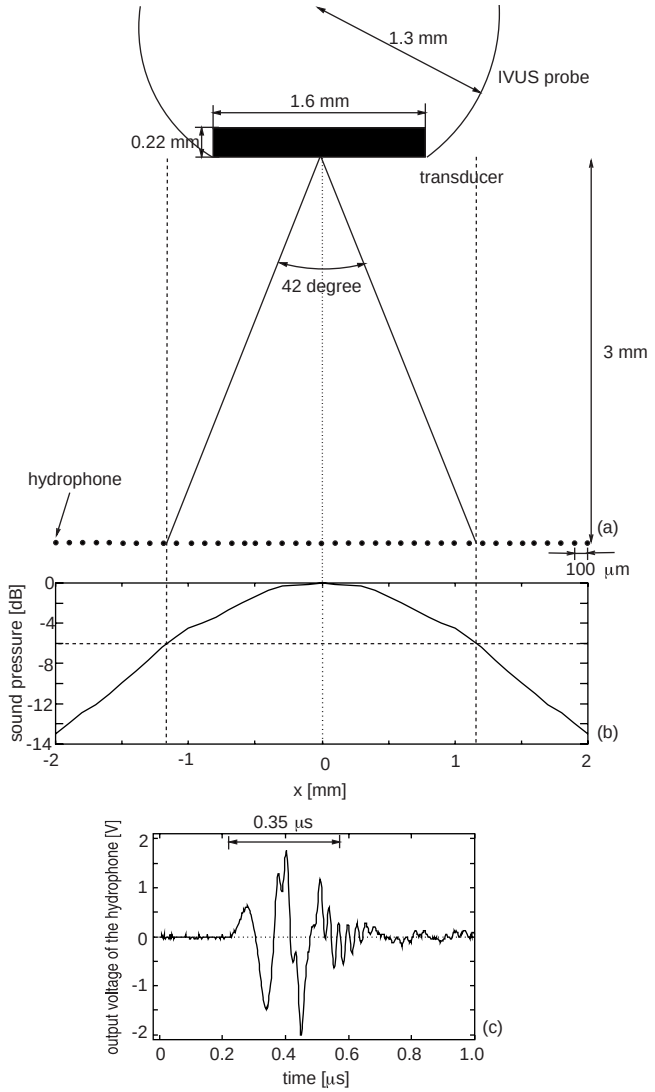

Fig. 9. Beam profile of the employed ultrasound. (a) Relationship between the positions of the IVUS transducer and the hydrophone. (b) Sound pressure of the employed ultrasound measured by moving the hydrophone at an interval of 100 μm for each point along the x-axis. (c) Waveform measured by the hydrophone at $x = 0$.

Fig. 9(a) and the sound pressure of the employed ultrasound is measured at each point as shown in Fig. 9(b). Based on these results, the aperture of the IVUS transducer is about 42°. Moreover, in order to measure the pulse width of the employed ultrasound, the output voltage of the hydrophone at $x = 0$ is measured and shown in Fig. 9(c). Based on this result, the pulse width of the ultrasound is 0.35 μs, which corresponds to 270 μm when the velocity of the object is approximately 1,540 m/s. From this pulse width, the window width δ employed in the calculation of the complex cross-correlation functions $C_{\text{in}}(t; P(r_0, \theta_0))$ in eq. (2.8) and $C_{\text{out}}(t; P(r_0, \theta_0))$ in eq. (2.9) is determined to be 300 μm in the following experiments. Since the width Δr along the ultrasonic beam of the small region around $P(r_0, \theta_0)$ should be equal to or larger than the window width δ, the thickness Δr is determined to be 300 μm in this experiment.

3. Basic Experiments using Silicone Rubber Tubes

3.1 Validation of the tracking operation

To validate the tracking operation described above, the IVUS probe is put into a silicone rubber tube as shown in Fig. 10 and the IVUS probe is moved manually by about 1 mm in the x–y plane. For the employed silicone rubber tube, the inner diameter and the outer diameter are 12 mm and 14 mm, respectively. A stainless steel needle is attached to the outer surface of the silicone rubber tube.

Figure 11 roughly shows the tracking results. The window width L in the radial direction in eq. (2.3) is 225 μm. The

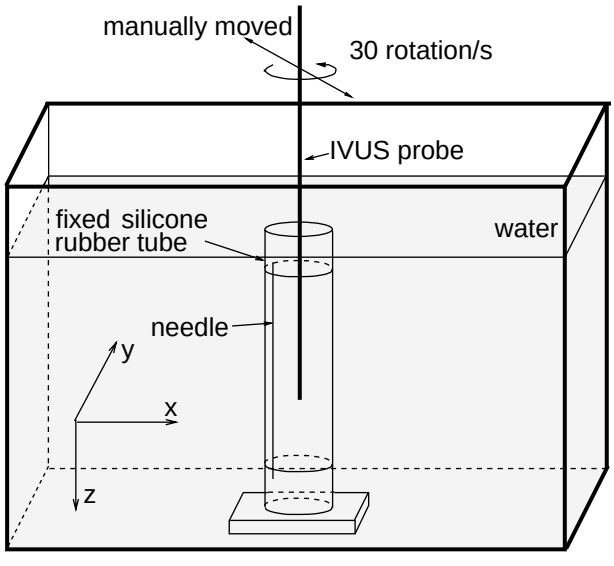

Fig. 10. Experimental setup for validating the tracking operation of the silicone rubber tube using a needle in a water tank.

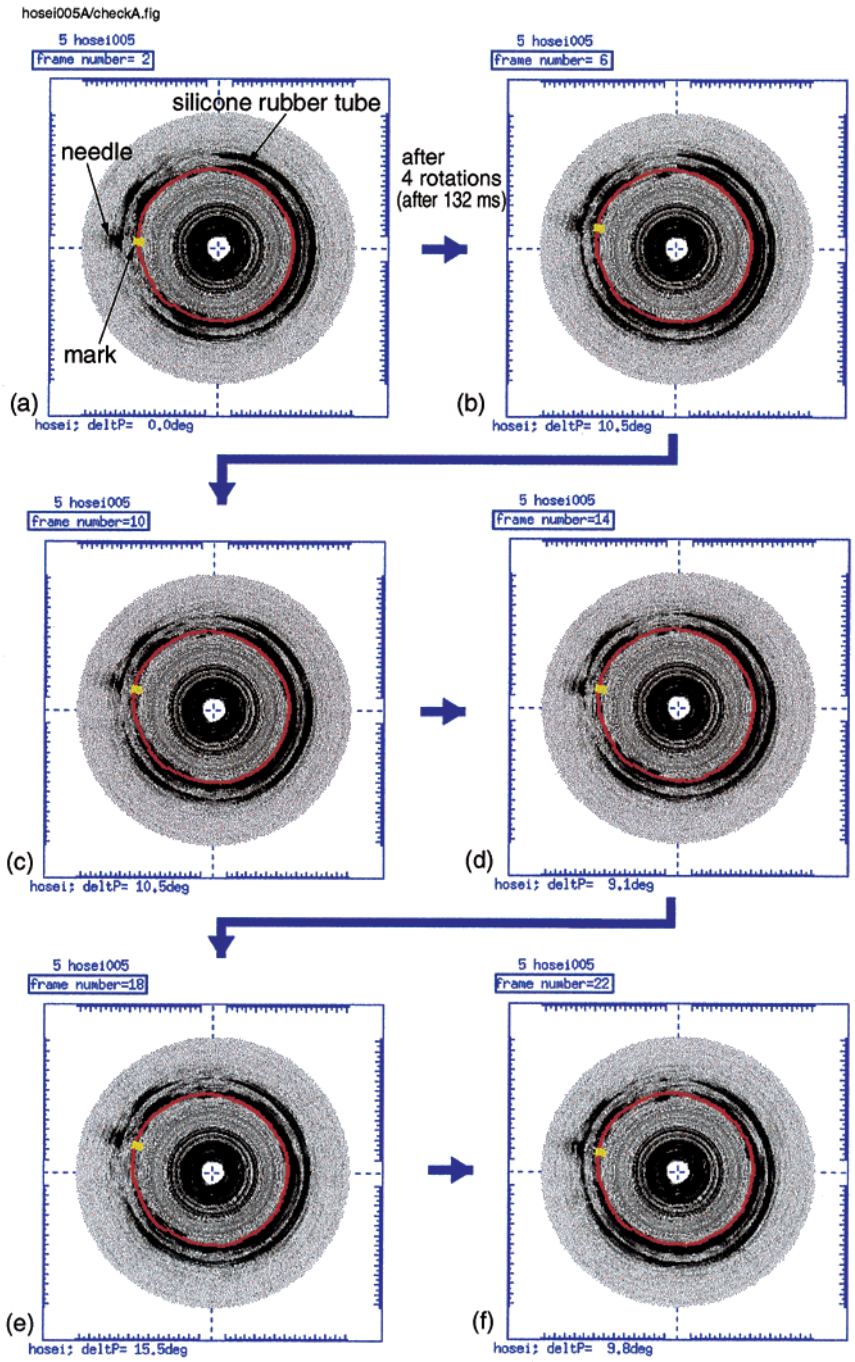

Fig. 11. Experimental results of the tracking operation, which is manually moved along the tube wall. From (a) to (f), the tracked results are displayed on the B-mode image at an interval of every $4th$ frame. The actual position of the needle along the wall is indicated by a blackend area and the estimated position of the needle is marked by a yellow dot.

tracking operation is applied continuously between successively obtained frames. The frame interval ΔT in eq. (2.3) is 33 ms. Typical frames are selected at an interval of 132 ms (every 4th rotation) and their B-mode images are shown in Figs. 11(a) to Fig. 11(f). The position of the needle is manually set at the first frame ($t = t_0$) and the estimates of the needle position (black point) are marked by a yellow dot in each of Figs. 11(a) to 11(f). The position of the needle is successfully tracked as shown in these figures.

3.2 Compensating for the inner pressure

In the following basic experiments, the regional change in thickness of a different silicone rubber tube, in which pulsatile flow is generated by an artificial heart, is measured using the same IVUS probe as that used in the experiments described above. Figure 12 shows the experimental setup. The silicone rubber tube has already been shown in Fig. 7. From eq. (2.23), the inner pressure p_B at point B is obtained from the pressure measurement p_A at point A and the velocity measurement v_C at point C.

3.3 Measuring the change in thickness and the elasticity

Using the experimental setup shown in Fig. 12, the instantaneous regional change in thickness, $\Delta h(t; P(r_0, \theta_0))$, of the silicone rubber tube caused by the pulsatile flow generated by the artificial heart is measured by the proposed method de-

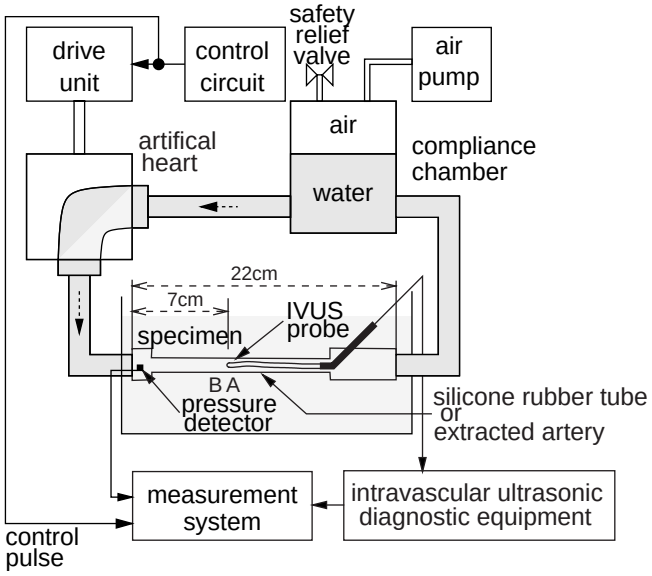

Fig. 12. Experimental setup using a silicone rubber tube or an extracted human iliac artery for an artificial circulatory system.

scribed above. The inner pressure p_A of the tube is simultaneously measured by the pressure sensor at point A in Figs. 7

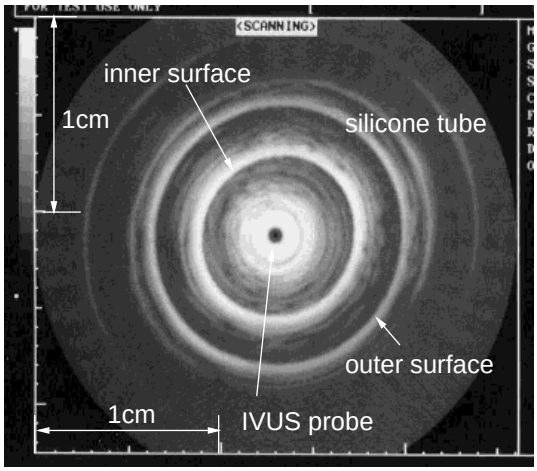

Fig. 13. Cross-sectional image of the silicone rubber tube (B-mode image) displayed by the intravascular ultrasonic equipment.

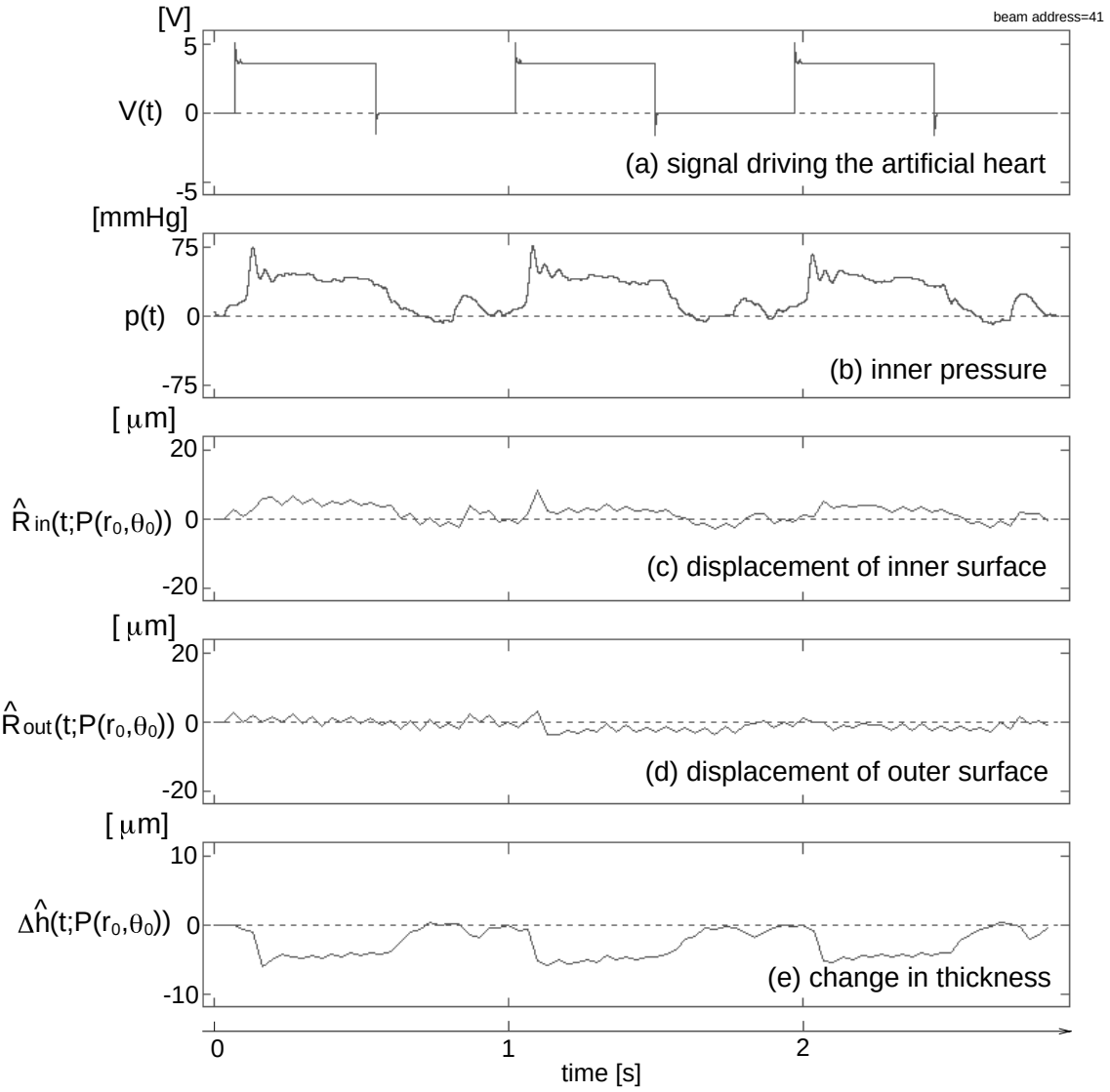

Fig. 14. The change in thickness of the silicone rubber tube in the artificial circulatory system of Fig. 12. (a) The signal driving the artificial heart. (b) The inner pressure of the silicone rubber tube. (c) The displacement of the inner surface of the tube wall. (d) The displacement of the outer surface of the tube wall. (e) The regional change in thickness of the tube obtained using the proposed method.

and 12. The employed silicone rubber tube is homogeneous and isotropic in elasticity, and the inner diameter and outer diameter are 8 mm and 11 mm, respectively. Figure 13 shows the cross-sectional image (B-mode image) of the employed silicone rubber tube displayed by the intravascular ultrasound equipment.

Figure 14(a) shows the driving signal of the artificial heart, by which pulsatile flow is generated in the silicone rubber tube. The inner pressure p_A of the tube measured by the pressure sensor is shown in Fig. 14(b). The inner pressure p_A increases due to the arrival of the pulsatile flow. Figures 14(c) and 14(d) show the instantaneous displacement of the inner surface of the tube and that of the outer surface of the tube, respectively. The instantaneous regional change in thickness, $\widehat{\Delta h}(t; P(r_0, \theta_0))$, of the tube estimated using eq. (2.3) is shown in Fig. 14(e) for $\theta_0 = 2.8°$ and $r_0 = 5.0$ mm. In this experiment, the window widths δ in the radial direction and ω in the circumferential direction obtained by calculating the complex cross-correlation functions, $C_{\text{in}}(t; P(r_0, \theta_0))$ in eq. (2.8) and $C_{\text{out}}(t; P(r_0, \theta_0))$ in eq. (2.9), are 300 μm and 21.7°, respectively, as described above. Thickness Δr of the small region is 1.5 mm. Although the change in thickness is very minute, there is reproducibility in the estimation of the change in thickness during three beats. The waveform of the estimation of the regional change in thickness, $\widehat{\Delta h}(t; P(r_0, \theta_0))$, in Fig. 14(e) is similar to that of the inner pressure p_A in the tube in Fig. 14(b) although they have mutually inverse polarity.

The instantaneous strain $\widehat{\varepsilon}_r(t; P(r_0, \theta_0))$ is obtained from the resultant change in thickness, $\widehat{\Delta h}(t; P(r_0, \theta_0))$, of the tube for each direction θ. Figure 15(a) shows the relationship between the inner pressure p_A and the estimation of the instantaneous strain, $\widehat{\varepsilon}_r(t; P(r_0, \theta_0))$, of the tube for $\theta_0 = 2.8°$.

To validate the results estimated by the proposed method using IVUS, we used a linear-type probe (7.5 MHz) in the conventional ultrasonic system (Toshiba, SSH-140A), and measured the change in thickness of the wall from the direction of $\theta = 0°$ (anterior wall) in a separate experiment based on the method developed by our group.[8] In this experiment, the IVUS probe maintains the same position in the silicone tube. The static pressure-strain relationship is shown in Fig. 15(b). The maximum of the inner pressure p_A at point A during the ejection period is corrected using eq. (2.23), as shown in Fig. 15(a).

From the average gradient, $\Delta p/\varepsilon_{\text{rm}}(r_0, \theta_0)$, which is denoted by the dotted lines in Fig. 15(a), the elastic modulus $E_\theta(r_0, \theta_0)$ in the circumferential direction obtained using eq. (2.17) is 2.7 MPa using the IVUS probe, and 2.4 MPa using the linear-type probe. From the separate static pressure-strain test shown in Fig. 15(b), the elastic modulus is 2.4 MPa. These values are almost the same.

In the same manner, the elastic modulus $E(r_0, \theta)$ is obtained for each direction θ ($0 \leq \theta < 2\pi$). Figure 16 shows the 2-D distribution of the elastic moduli $\{E_\theta(r_0, \theta)\}$ in the circumferential direction of the tube overlaid in the cross-sectional image. The measured elastic moduli are almost homogeneous in the circumferential direction θ. Their average value and the standard deviation are 2.7 MPa and 0.4 MPa, respectively.

According to reported values[11] of tissue elasticity, fibrous tissue is 4.1±5.1 MPa and normal tissue is 0.6±0.7 MPa. The difference in elasticity of fibrous tissue from that of normal tissue is much larger than the standard deviation (0.4 MPa) mentioned above using the proposed method. Thus, the 2-D distribution of the elastic modulus obtained by the proposed method has the potential to discriminate the different tissue properties.

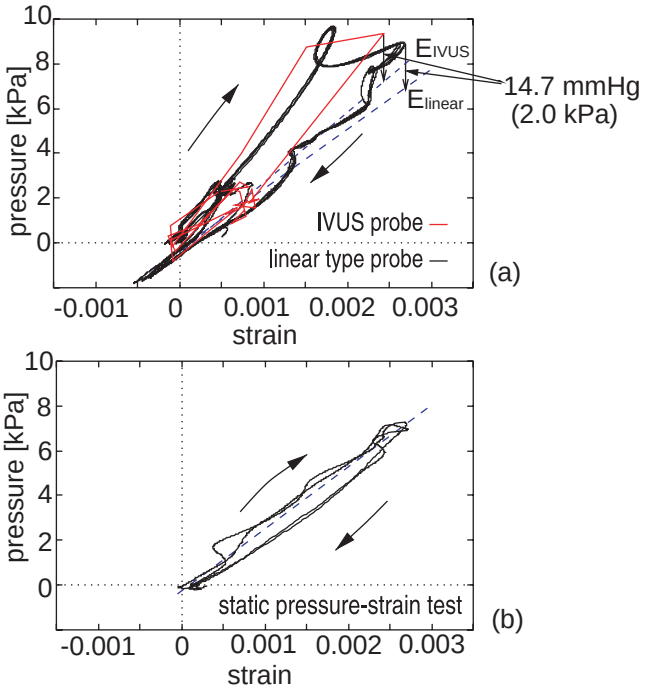

Fig. 15. Relationship between strain $\widehat{\varepsilon}_r(t; P(r_0, \theta_0))$ and pressure p_A. (a) The result obtained with the proposed method using the IVUS probe ($\theta_0 = 2.8°$) and a linear-type probe ($\theta_0 = 0°$). (b) The result obtaiend with the static pressure-strain test.

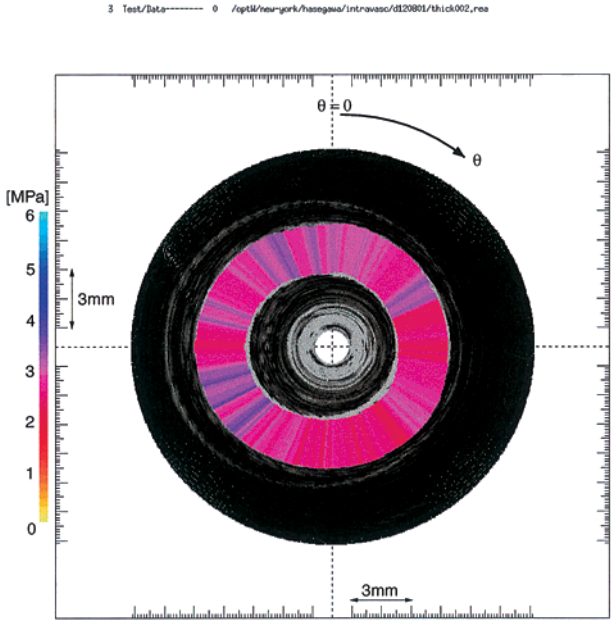

Fig. 16. 2-D distribution of the elastic moduli $\{E_\theta(r_0, \theta)\}$ of the silicone rubber tube.

4. *In vitro* Experiment using an Extracted Human Iliac Artery

Using the same experimental setup as the above basic experiment in Fig. 12, the elastic modulus of an extracted human iliac artery is measured by the proposed method. The thickness of the layer, Δr, is 300 μm and is equal to the window width δ of the complex cross-correlational function for estimating the phase shift. Figures 17(a) and 17(b) respectively show the 2-D distribution of the elastic moduli $\{E_\theta(r,\theta)\}$ measured by the proposed method and its pathological image, which is visualized by elastica-masson (EM) stain. The extracted artery is preserved in formalin immediatedly after the *in vitro* experiment and is visualized by EM stain. The EM stain dyes the collagen blue and the smooth muscle pink.

The region with the lipid plaque (A in Fig. 17) has an elasticity of 0.1–0.3 MPa and is elastically soft compared to the other regions in Fig. 17(a). On the other hand, the soft region (B in Fig. 17) corresponds to a blood clot and the stiff region (C in Fig. 17) corresponds to fibrous tissue. The measured elastic moduli $\{E_\theta(r,\theta)\}$ around the fibrous tissue is approximately 5.0–7.0 MPa, which corresponds to the reported value of the elasticity for the fibrous tissue of 4.1 ± 5.1 MPa.[11)]

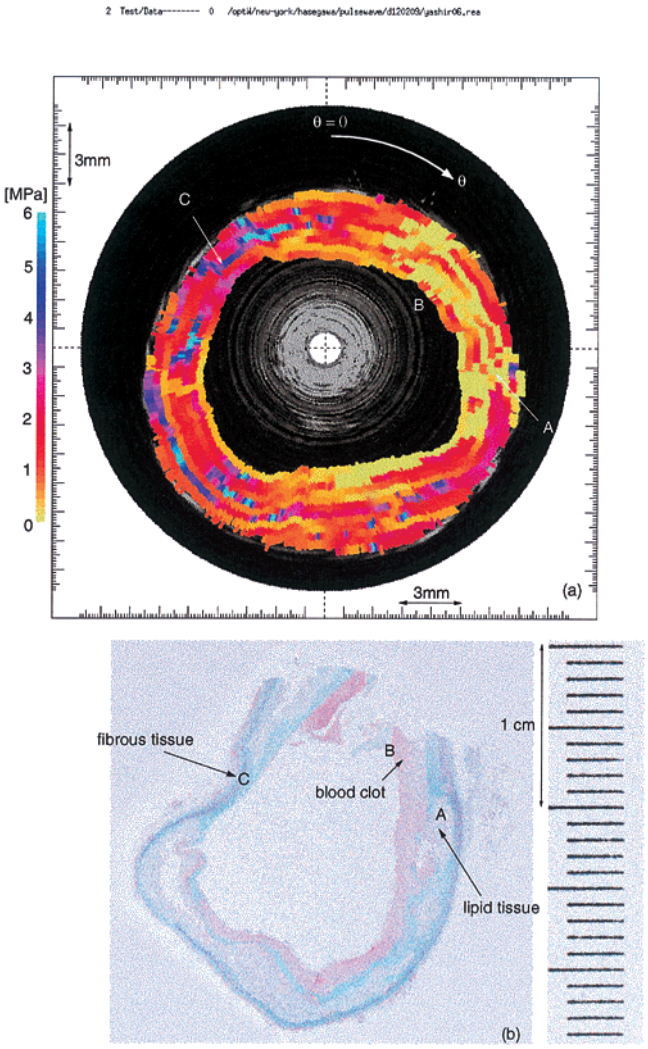

Fig. 17. Results of *in vitro* experiments using the extracted iliac artery. (a) The 2-D distribution of the elastic modulus. (b) The pathological image with EM staining.

5. Conclusions

In this experiment, we proposed a method for tracking the arterial wall in order to measure the regional change in thickness using IVUS. The proposed method was validated by the two basic experiments using two different silicone rubber tubes, and a cross-sectional image of the elasticity of the extracted human iliac artery was obtained in the *in vitro* experiment. The 2-D distribution of the elastic modulus had the potential for suppling useful information for the diagnosis of the vulnerability of atherosclerotic plaque.

It is well known that the elastic modulus of the arterial wall depends on blood pressure. In this experiment, it was assumed that the pressure dependence is negligible. For patients with hypertension, however, the pressure dependence should be compensated for. Further investigation of the proposed method, including this compensation and its clinical application to the local diagnosis of arterial disease and atherosclerosis, is being conducted.

Acknowledgments

We express appreciation to Mr. Keiji Kato and Mr. Kazuhiro Shiro of Aloka Co., Ltd., Japan for providing the IVUS equipment. Part of this work is supported by the Terumo Life Science Foundation.

1) R. T. Lee, A. J. Grodzinsky, E. H. Frank, R. D. Kamm and F. J. Schoen: Circulation **83** (1991) 1764.
2) M. K. Wolverson, H. M. Bashiti and G. J. Peterson: Ultrasound Med. & Biol. **9** (1983) 599.
3) C. L. de. Korte, A. F. W. van der Steen, E. I. Cespedes and G. Pasterkamp: Ultrasound Med. & Biol. **24** (1998) 401.
4) C. L. de Korte, S. G. Carlier, F. Mastik, M. M. Doyley, A. F. W. van der Steen, E. I. Cespedes, P. W. Serruys and N. Bom: 1999 IEEE Ultrasonics Symp. Proc., p. 1649.
5) E. I. Cespedes, C. L. de Korte and A. F. W. van der Steen: Ultrasound Med. & Biol. **26** (2000) 385.
6) C. L. de Korte, S. G. Carlier, F. Mastik, M. M. Doyley, A. F. W. van der Steen, E. I. Cespedes, P. W. Serruys and N. Bom: 1999 IEEE Ultrasonics Symp. Proc., p. 1649.
7) S. Oka: *Rheology* (Mokabo, Tokyo, 1986) [in Japanese].
8) H. Hasegawa, H. Kanai, N. Hoshimiya and Y. Koiwa: J. Med. Ultrason. **28** (2001) J3.
9) M. Hino: *Ryutai-Rikigaku* (Hydrodynamics) (Asakura-Syoten, Tokyo, 1992) [in Japanese].
10) K. Sunagawa, H. Kanai, Y. Koiwa, K. Nitta and M. Tanaka: 1999 IEEE Ultrasonics Symp. Proc., p. 1507.
11) H. M. Loree, A. J. Grodzinsky, S. Y. Park, L. J. Gibson and R. T. Lee: J. Biomech. **27** (1994) 195.